

Origin of nonlinear wake induced vibration

W.YAO · R.K.JAIMAN

Received: date / Accepted: date

Abstract We perform linear stability analysis (LSA) for the flow-induced vibration arranged in tandem configuration or wake induced vibration (WIV). The fluid reduced order model (ROM) is constructed by using an eigensystem realization algorithm (ERA) and coupled with a transversely vibrating bluff body in a state space format [13]. The WIV region and onset reduced velocity U_r can be predicted accurately by tracing the eigenvalue trajectories of the ROM for a range of U_r . The LSA reveals that the structure mode is the energy source to maintain WIV for $(Re, L) = (60, 2)$, where L is the streamwise distance of the two cylinders. The sharp corner of square cylinder is found to have the stabilizing effects, therefore, the WIV onset U_r is larger than its circular cylinder counterpart. The LSA shows that the circular cylinder WIV persists for $U_r \geq 6.1$, while the WIV of square cylinder terminates at $U_r \approx 19$ at $(Re, L) = (60, 2)$. The work extends our previous understanding of the vortex induced vibration (VIV) lock-in mechanism to WIV at low Reynolds number and provides an expolation of the origion of WIV and why it persists at certain conditons.

Keywords Nonlinear · Wake-induced-vibration · Model reduction

1 Introduction

vortex induced vibration (VIV) is a complex nonlinear coupling between the structure and the flow dynamic, which often results in large motion and reduce the structural fatigue life. VIVs have broad interests in the fields of offshore, wind, aerospace and energy harvesting engineering due to its richness in fluid physics. In VIV lock-in regime, the vortex shedding frequency deviates from the Strouhal law and lock on to the structure natural frequency. This freuqnacy lock-in phenomenon

W.YAO
National University of Singapore, now at Queen's University Belfast
E-mail: w.yao@qub.ac.uk

R.K.JAIMAN
National University of Singapore

is typically characterized by high structure amplitude and therefore has been an active topic over the past decade ([10,11,3]).

The commonly accepted interpretation of VIVs is attributed to the classical resonance, which depends on vortex shedding frequency (f_{vs}) matching structure natural frequency (f_N). However, numerical simulation has shown that the peak amplitude arises in the vicinity of lock-in onset rather than at $f_{vs}/f_N \approx 1$. Recently, Yao and Jaiman [13] developed an efficient VIV reduced order model (ROM) using eigensystem realization algorithm (ERA) and successfully performed linear stability analysis (LSA) of VIV system. The authors show that the lock-in onset of bluff bodies is triggered by unstable structure mode (SM), and the low frequency galloping is characterized by persisting unstable SM. The understanding of lock-in mechanism by ERA-based ROM paves a way to develop a feedback control strategy for VIVs suppression [12].

The wake induced vibration or WIV is considered as the flow induced vibration in tandem configuration. The nature of VIV and WIV arises similarly from wake instability. However, WIV has its particular physics feature. Based on spacing to diameter ratio (L/D), The tandem cylinder is characterized by three interference regimes [9,14,6]: proximity interference ($1 \leq L/D \leq 1.2$ to 1.8), wake interference ($1.8 \leq L/D \leq 3.4$ to 3.8) and no interference ($L/D \geq 3.8$). In proximity regime, the vortex shedding from the upstream cylinder is suppressed and the tandem bodyies behave like a single bluff body, whereas the flow becomes intricate in wake interference and shear layer reattachment, intermittent vortex shedding, etc gradually appear as L/D increases. The no interference regime is dominated by the co-shedding, where vortex shedding occurs separately from both the cylinders.

The downstream cylinder experiences large response persisting to high reduced velocity which is typically defined as wake induced galloping [4]. Recent work [2] dissociates the WIV from galloping concept. The authors argue the WIV is sustained by unsteady vortex shedding that provides energy to the WIV system, and has difference mechanism from VIV, which is considered as a *resonance* phenomenon. In another recent work [1], the authors provided a physical explanation for WIV by wake-stiffness concept. They argued that the wake-stiffness characterizes the WIV properties. The authors [2,1] insists that the WIV is a non-resonance fluid induced vibration (FIV) with increasing amplitude beyond frequency lock-in regime, and is mainly due to unsteady wake.

The paper is organized as follows. Section 2 introduces the FOM, ERA and ERA-based WIV ROM formulation in state space format. Section 3 describes the problem set-up. The LSA results are discussed in section 15b followed by conclusion in 15b.

2 Numerical methodology

2.1 Full-order model formulation

Consider the fluid domain $\Omega^f(t)$ with the spatial and temporal coordinates denoted by \mathbf{x}^f and t , respectively. The Navier-Stokes (NS) equations governing an

incompressible flow in the ALE reference frame are

$$\rho^f \left(\frac{\partial \mathbf{u}^f}{\partial t} \Big|_{\chi} + (\mathbf{u}^f - \mathbf{w}) \cdot \nabla \mathbf{u}^f \right) = \nabla \cdot \boldsymbol{\sigma}^f + \mathbf{b}^f \text{ on } \Omega^f(t), \quad (1)$$

$$\nabla \cdot \mathbf{u}^f = 0 \text{ on } \Omega^f(t), \quad (2)$$

where ρ^f , \mathbf{u}^f , \mathbf{w} , $\boldsymbol{\sigma}^f$, and \mathbf{b}^f are the fluid density, the fluid velocity, the ALE mesh velocity, the Cauchy stress tensor and the body force per unit mass, respectively. For the partial time derivative in Eq. (1), the ALE referential coordinate χ is held fixed and for a Newtonian fluid $\boldsymbol{\sigma}^f$ is defined as

$$\boldsymbol{\sigma}^f = -p\mathbf{I} + \mu^f \left(\nabla \mathbf{u}^f + (\nabla \mathbf{u}^f)^T \right), \quad (3)$$

where p , μ^f and \mathbf{I} are the pressure, the dynamic viscosity of the fluid and an identity tensor, respectively. The ALE mesh nodes on the fluid domain $\Omega^f(\mathbf{x}^f, t)$ can be updated by solving a linear steady pseudo-elastic material model

$$\nabla \cdot \boldsymbol{\sigma}^m = \mathbf{0}, \quad (4)$$

$$\boldsymbol{\sigma}^m = (1 + k_m) \left[\left(\nabla \boldsymbol{\eta}^f + (\nabla \boldsymbol{\eta}^f)^T \right) + (\nabla \cdot \boldsymbol{\eta}^f) \mathbf{I} \right], \quad (5)$$

where $\boldsymbol{\sigma}^m$ is the stress experienced by the ALE mesh due to the strain induced by the rigid-body movement, $\boldsymbol{\eta}^f$ represents the ALE mesh node displacement and k_m is a mesh stiffness variable chosen as a function of the element area to limit the distortion of small elements located in the immediate vicinity of the fluid-body interface. The fluid-structure coupling is achieved through a partitioned staggered procedure [7,13].

Given a base flow \mathbf{u}_0 , the corresponding linearized NS equations can be written in a semi-discrete form as [12],

$$\mathbf{E} \frac{d\mathbf{Q}}{dt} = \mathbf{F}\mathbf{Q}, \quad (6)$$

where the matrices and vectors in Eq. (6) are

$$\mathbf{F} = \begin{pmatrix} -() \cdot \nabla \mathbf{u}_0 - \mathbf{u}_0 \cdot \nabla () + \mu (\nabla () + \nabla^T ()) & -\nabla () \\ \nabla \cdot () & \mathbf{0} \end{pmatrix}, \quad (7a)$$

$$\mathbf{G} = \begin{pmatrix} () \cdot \nabla \mathbf{u}_0 & \mathbf{0} \\ \mathbf{0} & \mathbf{0} \end{pmatrix}, \mathbf{E} = \begin{pmatrix} \mathbf{I} & \mathbf{0} \\ \mathbf{0} & \mathbf{0} \end{pmatrix}, \mathbf{Q} = \begin{pmatrix} \mathbf{u} \\ p \end{pmatrix}. \quad (7b)$$

The forward and adjoint modes can be derived by solving generalized eigenvalue problem of linearized NS equation Eq. (6).

2.2 ERA-based model reduction

The linear time-invariant (LTI) and multiple-input multiple-output (MIMO) model represented in a state-space form at discrete times $t = k\Delta t$, $k = 0, 1, 2, \dots$, with a constant sampling time Δt reads

$$\left. \begin{array}{l} \mathbf{x}_r(k+1) = \mathbf{A}_r \mathbf{x}_r(k) + \mathbf{B}_r \mathbf{u}(k) \\ \mathbf{y}_r(k) = \mathbf{C}_r \mathbf{x}_r(k) + \mathbf{D}_r \mathbf{u}(k) \end{array} \right\}, \quad (8)$$

where \mathbf{x}_r is an n_r -dimensional state vector, \mathbf{u} denotes a q -dimensional input vector and \mathbf{y}_r is a p -dimensional output vector. The system matrices are $(\mathbf{A}_r, \mathbf{B}_r, \mathbf{C}_r, \mathbf{D}_r)$ convergence is derived from ERA method [8]. The detail procedure can be found in [13].

2.3 Reduced order model for WIV

In the present work, we only consider the transverse motion of cylinder for the sake of simplicity [13]. The structural governing equations can be expressed as,

$$\ddot{Y} + 4\zeta\pi F_s \dot{Y} + (2\pi F_s)^2 Y = \frac{a_s}{m^*} C_l, \quad (9)$$

where Y is the transverse displacement; C_l is the lift coefficient, m^* and ζ are the ratio of the mass of the vibrating structure to the mass of the displaced fluid and the damping coefficient, respectively; F_s is the reduced natural frequency of the structure defined as $F_s = f_N D/U = 1/U_r$, where U_r is the reduced velocity. $a_s = \frac{2}{\pi}$ for a circular cylinder, and $a_s = 0.5$ for a square cylinder. Equation (9) can be casted into space format as,

$$\dot{\mathbf{x}}_s = \mathbf{A}_s \mathbf{x}_s + \mathbf{B}_s C_l, \quad (10)$$

where the state matrices and vectors are

$$\mathbf{A}_s = \begin{bmatrix} 0 & 1 \\ -(2\pi F_s)^2 & -4\zeta\pi F_s \end{bmatrix}, \quad \mathbf{B}_s = \begin{bmatrix} 0 \\ \frac{a_s}{m^*} \end{bmatrix}, \quad \mathbf{x}_s = \begin{bmatrix} Y \\ \dot{Y} \end{bmatrix}.$$

The resultant fluid and structure coupled system ROM is formulated as,

$$\mathbf{x}_{fs}(k+1) = \begin{bmatrix} \mathbf{A}_{sd} + \mathbf{B}_{sd} \mathbf{D}_r \mathbf{C}_{sd} & \mathbf{B}_{sd} \mathbf{C}_r \\ \mathbf{B}_r \mathbf{C}_{sd} & \mathbf{A}_r \end{bmatrix} \mathbf{x}_{fs}(k) = \mathbf{A}_{fs} \mathbf{x}_{fs}(k), \quad (11)$$

where $\mathbf{A}_{sd} = e^{\mathbf{A}_s \Delta t}$, $\mathbf{B}_{sd} = \mathbf{A}_s^{-1} (e^{\mathbf{A}_s \Delta t} - \mathbf{I}) \mathbf{B}_s$.

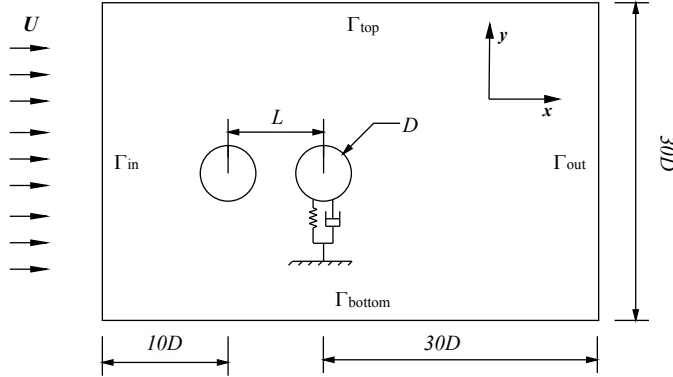


Fig. 1: Schematic diagram of a representative bluff body of elastically mounted cylinder in the wake of stationary cylinder. Computational domain and boundary conditions are shown.

3 Numerical set-up and verification

3.1 Problem definition

Similar to [13], figure 1 shows a schematic diagram of the setup used for WIV linear stability analysis. The coordinate origin is located at the center of the two bluff bodies. The streamwise and transverse directions are denoted x and y , respectively. A stream of incompressible fluid enters into the domain from an inlet boundary Γ_{in} at a horizontal velocity $(u, v) = (U, 0)$, where u and v denote the streamwise and transverse velocities, respectively. The downstream bluff body with mass m and characteristic diameter D is mounted on a linear spring in the transverse direction. The damping coefficient ζ is set to zero in the present work. The domain size is similarly set up as [13]. No-slip wall condition is implemented on the surfaces of the bluff body, and a traction-free boundary condition is implemented along the outlet Γ_{out} while the slip wall condition is implemented on the top Γ_{top} and bottom Γ_{bottom} boundaries. All length scales are normalized by the characteristic dimension D , velocities with the free stream velocity U , and frequencies with U/D . The Reynolds number Re of flow is based on the characteristic dimension D , kinematic viscosity of fluid and free-stream speed U . According to the mesh convergence study in [13], we consider the mesh consisting of 20912 $\mathbb{P}_2/\mathbb{P}_1$ isoparametric elements is sufficient for current WIV LSA study. The mesh is shown in figure 2 and the corresponding central rectangle represents the fine mesh region around the cylinder bodies. The mesh in the cylinder wake is appropriately refined to resolve the alternate vortex shedding.

3.2 Stationary tandem cylinder linear stability analysis

At $(Re, L) = (60, 2D)$, the WIV ERA-based ROM is first constructed for circular cylinder tandem configuration. The based flow, as shown in the figure 3, is computed via fixed point iteration without the time dependent term in the NS

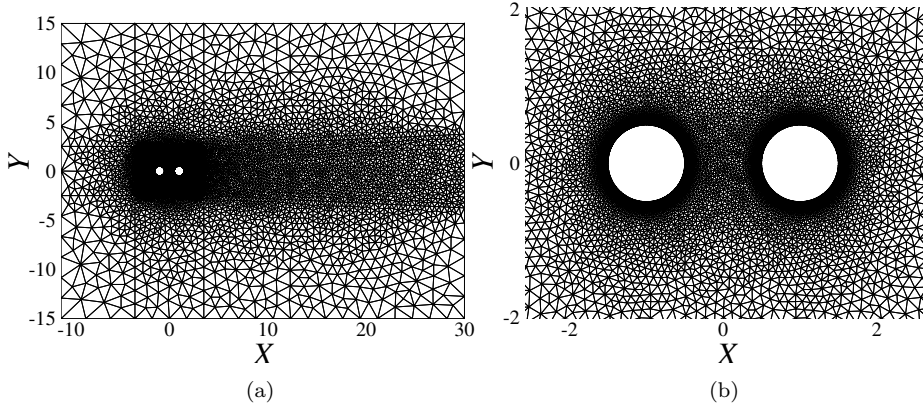


Fig. 2: Finite element mesh with $\mathbb{P}_2/\mathbb{P}_1$ discretization: (a) full domain discretization and (b) close-up view of in the vicinity of the tandem cylinder.

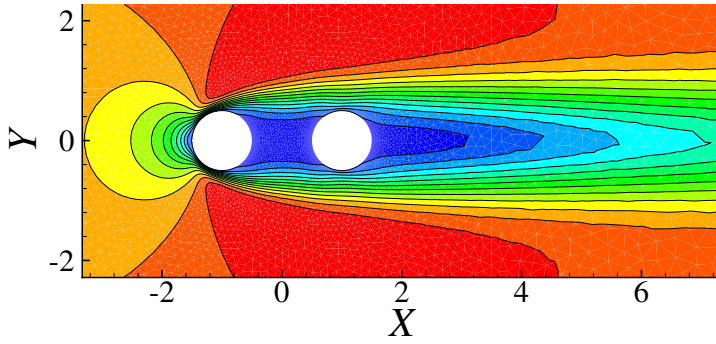


Fig. 3: Base flow of tandem circular cylinder at $(Re, L) = (60, 2D)$; The streamwise velocity contours are shown. The contour levels are from -0.1 to 1.2 in increments of 0.1.

equation. Following the ERA-based ROM construction procedure in [13], 1000 impulse outputs (C_l) are stacked by imposing $\delta(t) = 10^{-4}$ on the transverse displacement Y of downstream cylinder with time step size $\Delta t = 0.05$. Subsequently, 25^{th} ROM is determined by examining the decaying singular value of Hankel matrix [8]. A good match between FOM and 25^{th} ROM is found in figure 4. The impulse response gradually decays and indicates that real part of the least damped eigenvalue is negative and the uncoupled fluid system is stable. The least damped eigenvalue predicted by ERA-based ROM is compared with FOM in figure 5. The FOM results are derived by solving a generalized eigenvalue problem of Eq. (6).

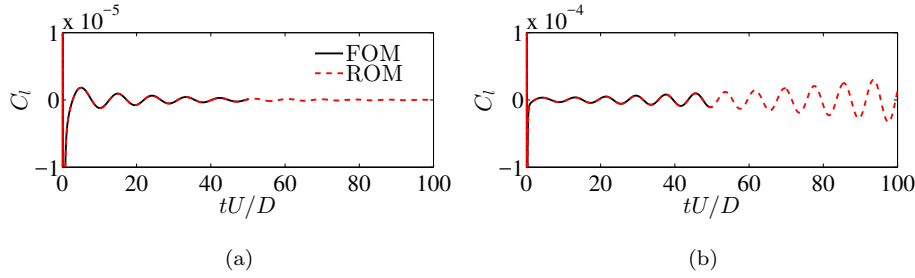


Fig. 4: The lift coefficient history of the 25th ROM compared with FOM subject to the impulse response. (a) $Re = 60$. (b) $Re = 120$.

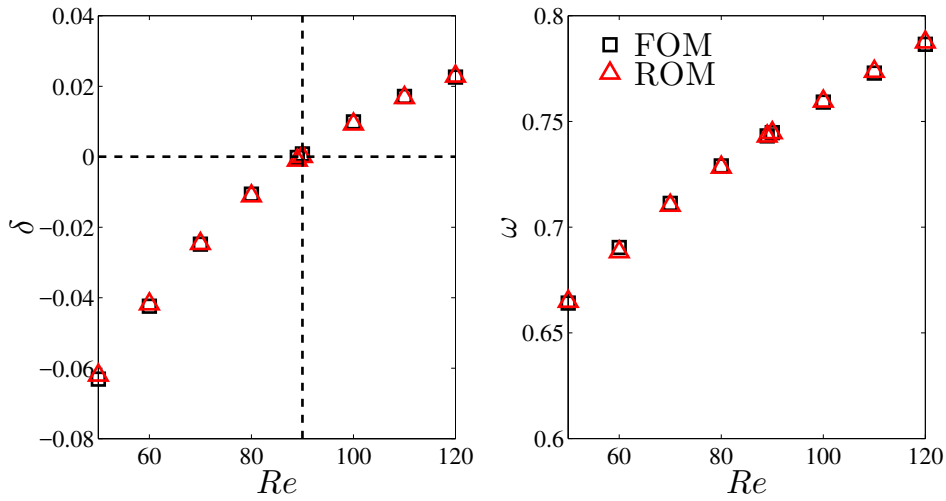


Fig. 5: The growth rate and frequency of the least damped eigenvalue for the flow past a tandem circular cylinder with $L = 2D$: (a) growth rate σ and (b) frequency ω . The cylinder wake becomes unstable when the growth rate crosses $\sigma = 0$ line at the critical $Re_{cr} \approx 90$ and the vortex shedding emanates.

4 Results and discussion

4.1 WIV of circular cylinder

Figure 6 shows the root loci of the WIV ERA-based ROM as a function of reduced velocity U_r with $2 \leq U_r \leq 40$. Following previous work in [13], the terminology WMI and WMII are adopted to classify the eigenvalue branches. As can be seen, the WMII branch arises from the high frequency region or the top of the complex plane, while the WMI branch originates from the uncoupled mode and travels down to the low frequency or bottom of the complex plane. As elucidated in the

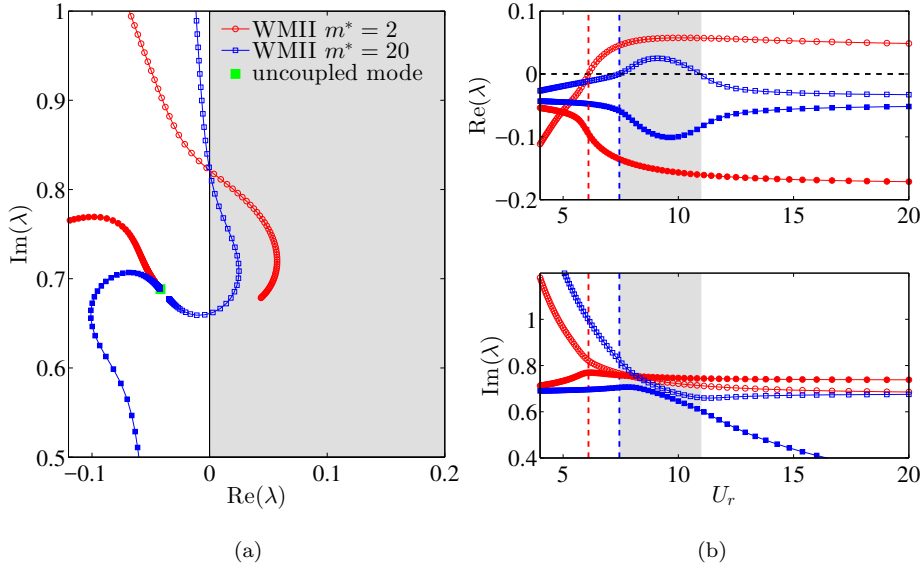


Fig. 6: Eigenspectrum of the ERA-based ROM at $(Re, L) = (60, 2D)$: (a) root loci as a function of the reduced velocity U_r , where the unstable right-half ($\text{Re}(\lambda) > 0$) plane is shaded in grey color. The WMI is denoted by filled symbols with the same shape as those for the WMII. The uncoupled wake mode $\lambda = -0.042 + 0.69i$. (b) Real and imaginary parts of the root loci at $(Re, L) = (60, 2D)$. The WIV region at $m^* = 20$ is shaded in grey colour, which is defined by $7.44 \leq U_r \leq 11.0$. - - - and - - - - represent WIV onset $U_r \approx 6.1$ and $U_r \approx 7.44$ for $m^* = (2, 20)$, respectively.

figure 6, the real part of WMII branch remains unstable when $U_r \geq 6.1$ and WMI branch is stable, which indicates the WIV persists at $m^* = 2$. The finding is further confirmed by the FOM in figure 16, where the WIV onset $U_r = 5.9$ and the WIV remains for $U_r \geq 5.9$. Figure 6 shows that the WMI branch is only unstable when $7.44 \leq U_r \leq 11.0$ at $m^* = 20$, which is evident from the figure 16. Furthermore, in figure 6(b) (bottom), the $\text{Im}(\lambda)$ plot shows the characteristic anticrossing between WMI and WMII for the low mass ratio $m^* = 2$. This intrinsic property of strong coupling system is also found for single cylinder VIV system at low mass ration [13]. The two counter-rotating vortices (2S mode) are released at onset $U_r = 5.9$ and $(Re, m^*, L) = (60, 2, 2D)$ as shown in figure 8. The figure 9 and 10 depict the transverse displacement and lift traces with the corresponding spectrum, which confirms the high harmonid response of WIV.

Apart from the unstable eigenvalue branches, it is also interesting to see the WIV from the engery transfer viewpoint. The engery transfer over one period T for WIV system is derived as equation 14 in Appendix A. The E_c is defined by excluding the exponential growth/decay rate. The figure 11 suggests that energy source to sustain the WIV is the unstable WMII at $(Re, L) = (60, 2D)$.

As shown 12, the uncoupled mode moves to the right half-complex-plane at $Re = 100$. Compared with root loci at $Re = 60$, figure 12 shows that the eigenvalue branches moves to high frequency regime or upper part of complex plane. The onset

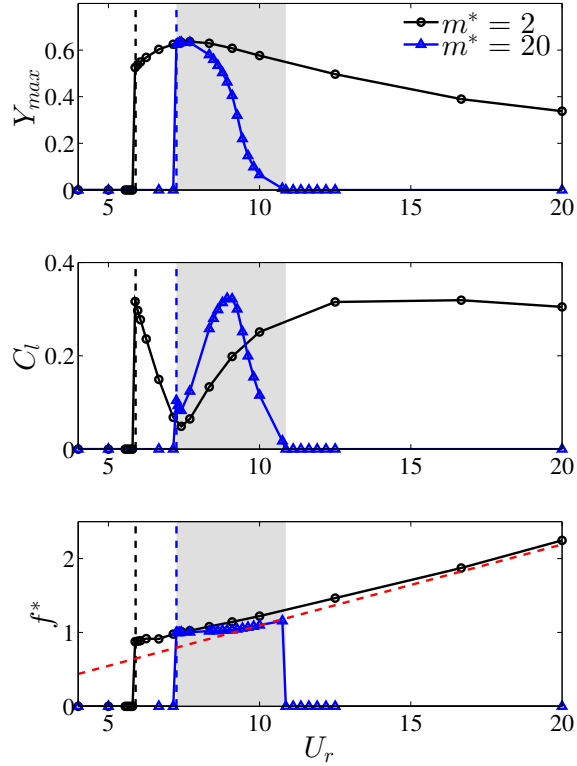


Fig. 7: Normalized maximum amplitude Y_{max} and rms value of lift coefficient C_l as a function of reduced velocity U_r at $(L, Re) = (2D, 60)$. The WIV region $7.25 \leq U_r \leq 10.87$ at $m^* = 20$ is shaded in grey colour. - - - and - - - - represent WIV onset $U_r = 5.9$ and $U_r = 7.25$, respectively. - - - is the uncoupled mode frequency predicted by ROM.

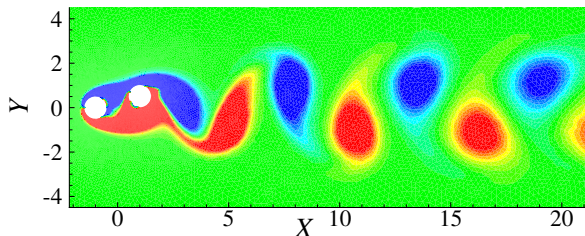


Fig. 8: Instantaneous vorticity contours of WIV onset ($U_r = 7.25$) at $(Re, m^*, L) = (60, 2, 2D)$. The contour levels are from 0.5 to 0.5 in increments of 0.067 and the flow is from left to right.

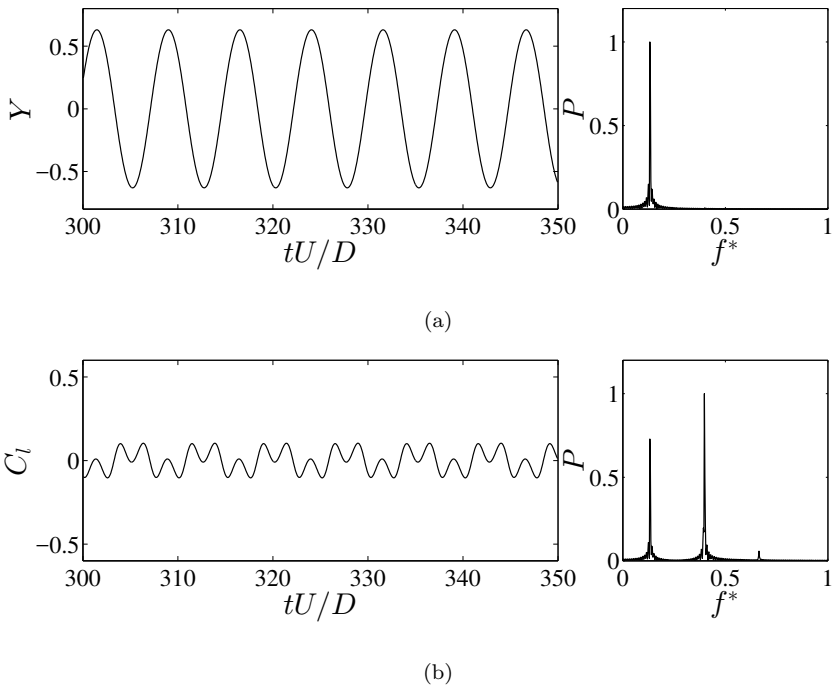


Fig. 9: FOM results of circular WIV at $(Re, m^*, L) = (60, 2, 2D)$: temporal variation of (a) transverse amplitude, and (b) lift coefficient; normalized power spectrum P versus f^* of: (a) transverse amplitude, (b) lift coefficient at reduced velocity $U_r \approx 7.69$ or $F_s = 0.13$, where $f^* = f/F_s$ is the frequency of lift and transverse displacement normalized by reduced natural frequency F_s . A third-harmonic frequency is evident in C_l .

U_r of WIV predicted by ERA-based ROM is at $U_r \approx 5.4$. Figure 17 shows the instantaneous vortex structure at onset reduced velocity $U_r \approx 5.3$ which shows C(2S) pattern.

4.2 WIV of square cylinder

In this section, we further explore the WIV of square cylinder. In our previous work [13], we demonstrate that the sharp corner has stabilizing effects for fluid structure coupling. Thereofre, It is interesting to investigate the WIV mechanism of square cylinder by means of ERA-based ROM. The flow region with high sensitivity and strong response or wavemaker region is determined by computing the pointwise product of the forward and adjoint global modes [5]. Figure 14 shows that the wavemaker region of the circular tandem cylinder has higher value and moves closer to the cylinders than its circular counterpart, which suggests that the circular tandem cylinder has stronger fluid and structure interation level.

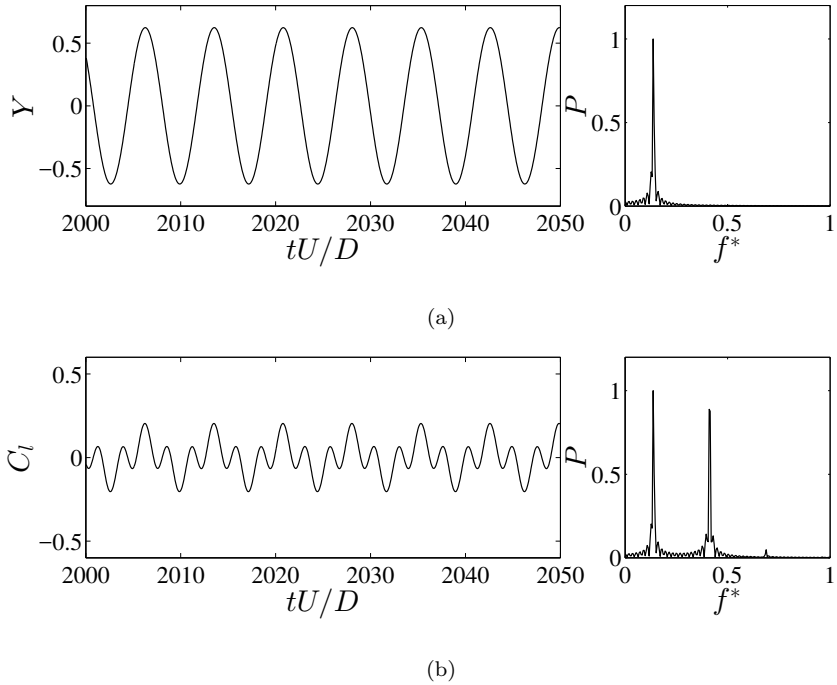


Fig. 10: FOM results of circular WIV at $(Re, m^*, L) = (60, 20, 2D)$: temporal variation of (a) transverse amplitude, and (b) lift coefficient; normalized power spectrum P versus f^* of: (a) transverse amplitude, (b) lift coefficient at onset reduced velocity $U_r \approx 7.25$ or $F_s = 0.138$, where $f^* = f/F_s$ is the frequency of lift and transverse displacement normalized by reduced natural frequency F_s . A third-harmonic frequency is evident in C_l .

5 Concluding remarks

Appendix A: Energy Transfer for WIV

Following our previous work on VIV [13], the displacement and lift coefficient can be obtained for the WIV linear system as,

$$\left. \begin{aligned} Y &= \hat{Y} e^{\lambda_r t} \cos(\lambda_i t) \\ C_l &= \hat{C}_l e^{\lambda_r t} \cos(\lambda_i t + \phi) \end{aligned} \right\}, \quad (12)$$

where $\lambda = \lambda_r + i\lambda_i$ is eigenvalue with real λ_r and imaginary λ_i components, \hat{Y} and \hat{C}_l denote the magnitudes of eigenmodes. The phase angle difference is derived by plugging the Eq. (12) into Eq. (9), and refer to [13] for details.

$$\sin \phi = \frac{2\lambda_r \lambda_i}{\sqrt{(\lambda_r^2 + (2\pi F_s)^2 + \lambda_i^2)^2 - (4\pi \lambda_i F_s)^2}}. \quad (13)$$

The energy transfer per cycle is defined as,

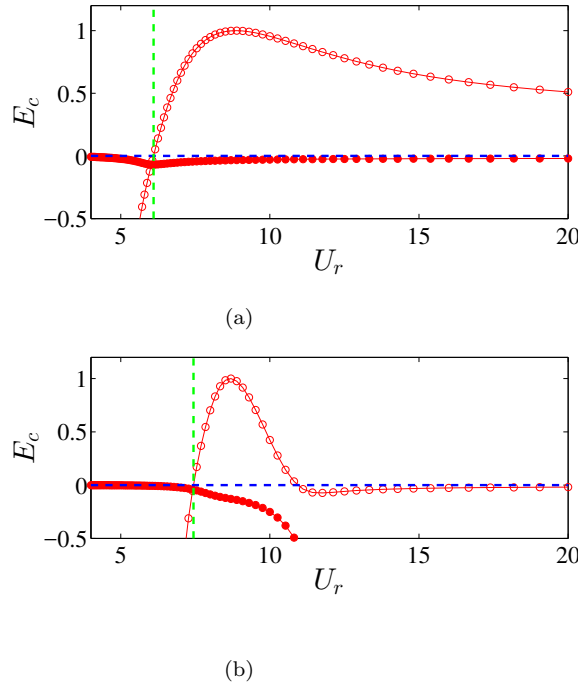


Fig. 11: E_c as a function of reduced velocity U_r at $(L, Re) = (2D, 60)$. (a) $m^* = 2$, and (b) $m^* = 20$. --- represents the onset reduced velocity U_r .

$$\begin{aligned} E(t) &= \int_t^{t+\frac{2\pi}{\lambda_i}} \dot{Y} \hat{C}_l dt \\ &= \frac{1}{2} (\lambda_i \sin(\phi) + \lambda_r \cos(\phi) + \lambda_r \cos(2\lambda_i t + \phi)) \int_t^{t+\frac{2\pi}{\lambda_i}} e^{2\lambda_r t} dt \end{aligned} \quad (14)$$

E_c is defined by excluding the exponential growth/decay rate λ_r in Eq. (14),

$$E_c = \pi \dot{Y} \hat{C}_l \sin(\phi) \quad (15)$$

References

- Assi, G.R.S., Bearman, P.W., Carmo, B.S., Meneghini, J.R., Sherwin, S.J., Willden, R.H.J.: The role of wake stiffness on the wake-induced vibration of the downstream cylinder of a tandem pair. *Journal of Fluid Mechanics* **718**, 210245 (2013). DOI 10.1017/jfm.2012.606
- ASSI, G.R.S., BEARMAN, P.W., MENEGHINI, J.R.: On the wake-induced vibration of tandem circular cylinders: the vortex interaction excitation mechanism. *Journal of Fluid Mechanics* **661**, 365401 (2010). DOI 10.1017/S0022112010003095
- Bearman, P.W.: Circular cylinder wakes and vortex-induced vibrations. *Journal of Fluids and Structures* **27**(5), 648–658 (2011)
- Bokaian, A., Geoola, F.: Wake-induced galloping of two interfering circular cylinders. *Journal of Fluid Mechanics* **146**, 383415 (1984). DOI 10.1017/S0022112084001920

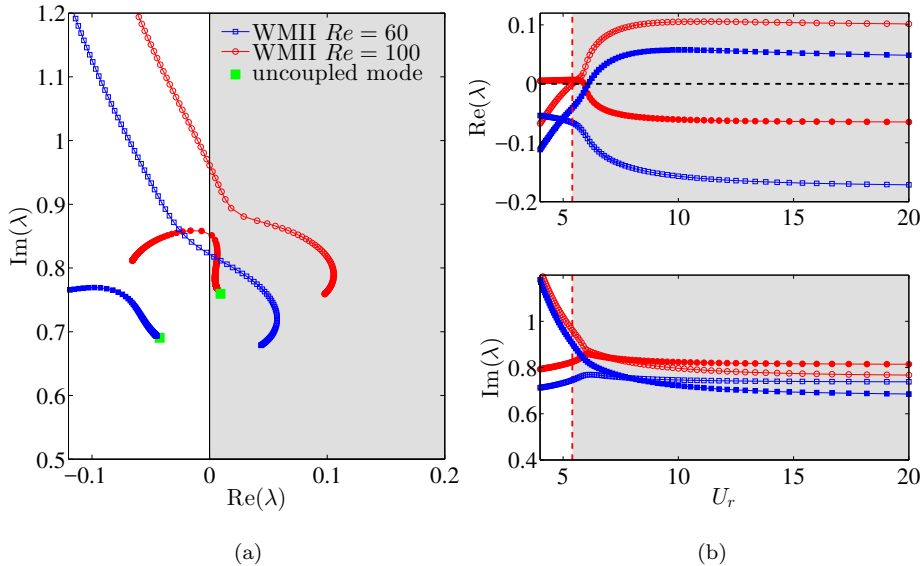


Fig. 12: Eigenspectrum of the ERA-based ROM at $(m^*, L) = (2, 2D)$: (a) root loci as a function of the reduced velocity U_r , where the unstable right-half ($\text{Re}(\lambda) > 0$) plane is shaded in grey color. The WMI is denoted by filled symbols with the same shape as those for the WMII. The uncoupled wake mode $\lambda = 0.01 + 0.759i$. (b) Real and imaginary parts of the root loci at $(Re, L) = (100, 2D)$. The WIV region at $(Re, m^*) = (100, 2)$ is shaded in grey colour, which is defined by $U_r \geq 5.4$.

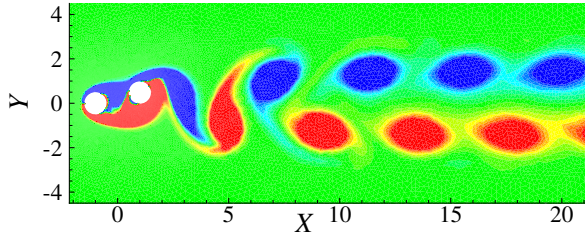


Fig. 13: Instantaneous vorticity contours of WIV onset ($U_r = 5.3$) at $(Re, m^*, L) = (100, 2, 2D)$. The contour levels are from 0.5 to 0.5 in increments of 0.067 and the flow is from left to right.

5. Giannetti, F., Luchini, P.: Structural sensitivity of the first instability of the cylinder wake. *Journal of Fluid Mechanics* **581**, 167–197 (2007)
6. Igarashi, T.: Characteristics of the flow around two circular cylinders arranged in tandem : 1st report. *Bulletin of JSME* **24**(188), 323–331 (1981). DOI 10.1299/jsme1958.24.323
7. Jaiman, R.K., Geubelle, P., Loth, E., Jiao, X.: Transient fluid-structure interaction with non-matching spatial and temporal discretizations. *Computers and Fluids* **50**, 120–135 (2011)
8. Juang, J.N., Pappa, R.S.: An Eigensystem Realization Algorithm for Modal Parameter Identification and Model Reduction. *J. Guidance* **8**(5), 620–627 (1985)

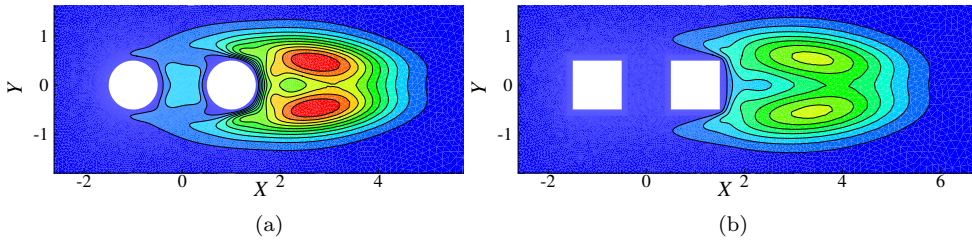


Fig. 14: Wavemaker region of (a) circular and (b) square cylinder at $(Re, L) = (60, 2D)$. The contour levels are from 0.04 to 0.35 in increments of 0.035 and the flow is from left to right.

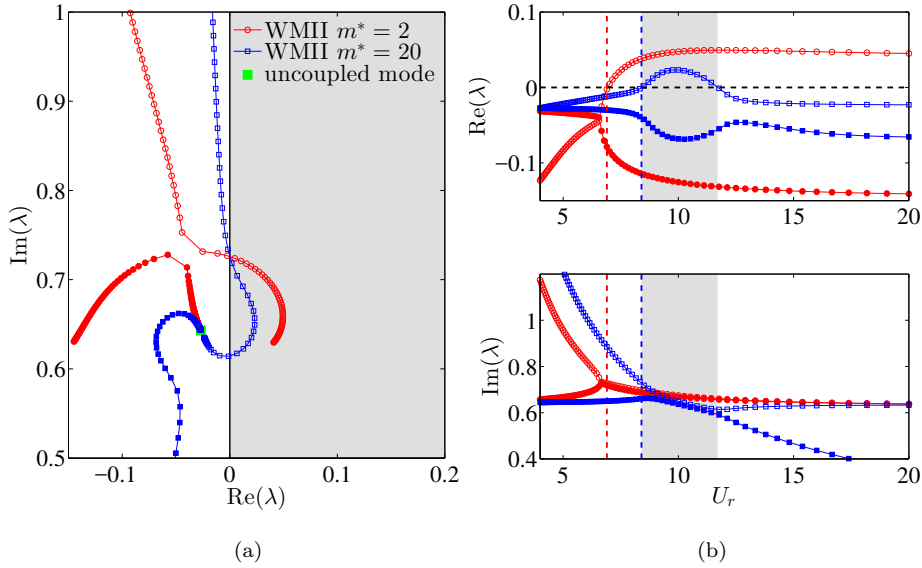


Fig. 15: Eigenspectrum of the ERA-based ROM at $(Re, L) = (60, 2D)$: (a) root loci as a function of the reduced velocity U_r , where the unstable right-half ($\text{Re}(\lambda) > 0$) plane is shaded in grey color. The WMI is denoted by filled symbols with the same shape as those for the WMII. The uncoupled wake mode $\lambda = -0.027 + 0.643i$. (b) Real and imaginary parts of the root loci at $(Re, L) = (60, 2D)$. The WIV region at $m^* = 20$ is shaded in grey colour, which is defined by $8.4 \leq U_r \leq 11.7$. - - - and - - - - represent WIV onset $U_r = 6.75$ and $U_r = 8.4$ for $m^* = (2, 20)$, respectively.

9. Mysa, R.C., Kaboudian, A., Jaiman, R.K.: On the origin of wake-induced vibration in two tandem circular cylinders at low Reynolds number. *Journal of Fluids and Structures* **61**, 76–98 (2016)
10. Sarpkaya, T.: A critical review of the intrinsic nature of vortex-induced vibrations. *Journal of Fluids and Structures* **19**(4), 389–447 (2004)
11. Williamson, C.H.K., Govardhan, R.: Vortex-induced vibrations. *Annual Review of Fluid Mechanics* **36**, 413–455 (2004)

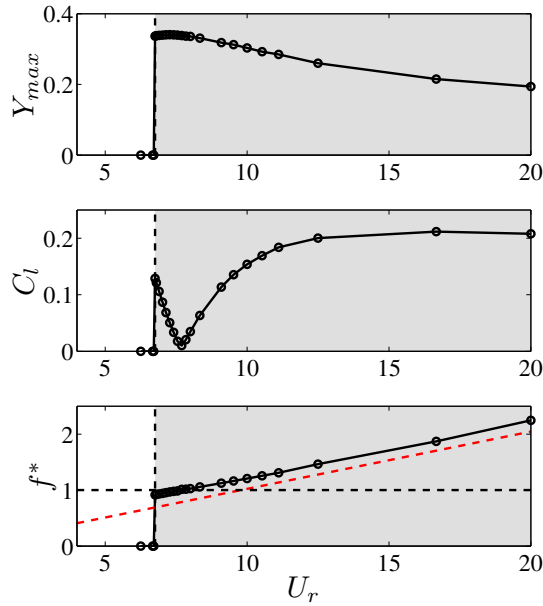


Fig. 16: Normalized maximum amplitude Y_{max} and rms value of lift coefficient C_l as a function of reduced velocity U_r at $(L, Re, m^*) = (2D, 60, 2)$. The WIV region is shaded in grey colour. - - - represents WIV onset $U_r = 6.76$. - - - - is the uncoupled WM frequency predicted by ROM.

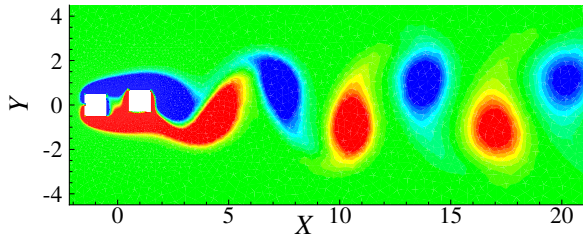


Fig. 17: Instantaneous vorticity contours of WIV onset ($U_r = 6.76$) at $(L, Re, m^*) = (2D, 60, 2)$. The contour levels are from 0.5 to 0.5 in increments of 0.067 and the flow is from left to right.

12. Yao, W., Jaiman, R.K.: Feedback control of unstable flow and vortex-induced vibration using the eigensystem realization algorithm. *Journal of Fluid Mechanics* **827**, 394414 (2017). DOI 10.1017/jfm.2017.470
13. Yao, W., Jaiman, R.K.: Model reduction and mechanism for the vortex-induced vibrations of bluff bodies. *Journal of Fluid Mechanics* **827**, 357393 (2017). DOI 10.1017/jfm.2017.525
14. Zdravkovich, M.: The effects of interference between circular cylinders in cross flow. *Journal of Fluids and Structures* **1**(2), 239 – 261 (1987)